

## Research Article

# The Role of Isostasy in the Evolution and Architecture of Fold and Thrust Belts

Youseph Ibrahim  and Patrice F. Rey

*Earthbyte Research Group, School of Geosciences, University of Sydney, Sydney, NSW 2006, Australia*

Correspondence should be addressed to Youseph Ibrahim; [youseph.ibrahim@sydney.edu.au](mailto:youseph.ibrahim@sydney.edu.au)

Received 13 June 2022; Revised 3 January 2023; Accepted 10 January 2023; Published 4 February 2023

Academic Editor: Feng Cheng

Copyright © 2023 Youseph Ibrahim and Patrice F. Rey. Exclusive Licensee GeoScienceWorld. Distributed under a Creative Commons Attribution License (CC BY 4.0).

Warmer conditions prevalent in the hinterland of orogenic systems facilitate local ductile flow underneath the surface load, making Airy-like local isostasy more prevalent in these domains. In contrast, flexural isostasy better describes the regional response to surface loading of more rigid lithospheres. Here, we explore how the interaction between horizontal tectonic mass transfer and vertical isostatic mass transfer, through either elastic flexure or viscous flow, impacts the overall architecture of fold and thrust belts. We compare numerical models of fold and thrust belts under either an Airy-like ductile isostasy boundary condition or a flexural-like regional isostasy boundary condition. Our experiments suggest that when ductile flow is involved in accommodating isostatic adjustment, subsidence is rather local, larger, and results in narrower, less elevated fold-thrust belts with a complex internal architecture consisting of prominent steeply dipping faults. When isostatic subsidence is controlled by lithospheric flexure, the tilting of the basement on 10 s of km scale facilitates the outward propagation of fold-thrust belts. The internal architecture is simpler and involves prominent basement-parallel décollements. The outcome is wider fold and thrust belts with higher topographies. A change in lithospheric elastic thickness does not significantly affect fold-thrust belt structural styles. Our results are compared to natural examples from the Subandean zone.

## 1. Introduction

Fold-thrust belts (FTB) form at plate convergent boundaries, often adjacent to a cordillera or a collisional orogen or adjacent to a subduction zone as part of an accretionary wedge. FTBs develop within a dynamic framework in which tectonic processes, surface processes, and isostatic processes interact under rock mechanical properties that evolve in response to temperature, strain, and fluid-rock interactions. Their development has been well-studied through analog and numerical experiments (e.g., [1–7]). These studies show that the architecture of an FTB is influenced by many processes including convergence rate, preexisting basement structures [8], the mechanical stratigraphy of the sedimentary pile [9], and surface processes [10–12]. During the build-up of an FTB, tectonic and sedimentary loading along with the critical taper angle [13] controls the internal deformation of the wedge [14]. The increasing load further influences FTB architecture by forcing local subsidence and/or

more regional plate bending, which provides accommodation space for further sedimentation, lowers the surface slope, and increases the height of the wedge. Hence, the bending and subsidence of the surface supporting the load are of critical importance.

When numerical experiments aim to study high-resolution small-scale FTB development, the model domain is generally computationally restricted to the upper crust. Therefore, modellers forego processes that occur underneath the model such as isostasy (Figure 1), that may influence the evolution of an FTB. As a result, numerical experiments are often run with a rigid model base. An alternative approach is to employ a boundary condition at the base of the model that simulates processes occurring underneath the model domain.

In numerical experiments involving loading or unloading of the Earth's surface, isostasy can be implemented following two approaches. Assuming that the flexural response of the lithosphere can be described by a model involving an ideal

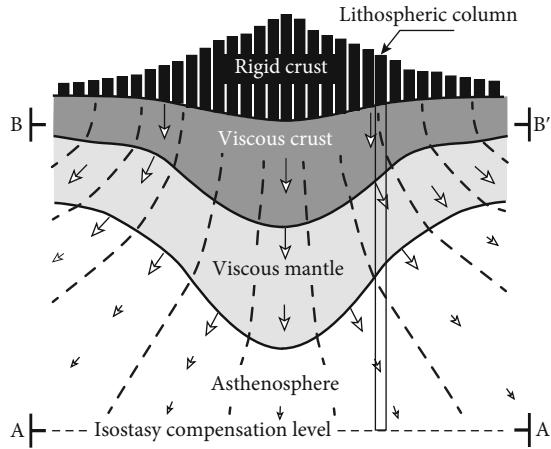


FIGURE 1: According to Airy isostasy, the isostatic subsidence or uplift of a lithospheric column following loading of its surface maintains the pressure at the compensation level ( $A-A'$ ) laterally constant. In contrast, the tempo of isostasy and its wavelength depend on the entire viscosity field. To achieve self-consistent isostasy and to capture enough structural details at the scale of sedimentary basins, computational grid needs not only to capture the entire viscosity flow field down to the compensation level but also to do so at a resolution  $< 100$  m. This is computationally not doable. Here, we implement a boundary condition underneath the basin (profile  $B-B'$ ) that allow us to explore the effect of the magnitude and wavelength of Airy-like subsidence.

elastic plate overlaying an inviscid fluid [6, 15–17], the magnitude of flexure, which is assumed to be quasi-instantaneous, depends on the material properties of the elastic plate and its elastic thickness. In many numerical experiments, it is implemented via GFlex, a python library that calculates at each timestep the amount of vertical motion due to the surface load distribution [18]. In this model, the lithosphere is represented by an ideal elastic plate of fixed elastic rigidity ( $D$ ):

$$D = \frac{ET_e^3}{12(1-\nu^2)}, \quad (1)$$

where  $E$  is Young's modulus,  $T_e$  is the lithospheric elastic thickness, and  $\nu$  is Poisson's ratio. In one-dimension, the plate flexure ( $w$ ) under a surface point load ( $q$ ) is then given by solving

$$D \frac{d^4 w}{dx^4} + \Delta \rho g w = q. \quad (2)$$

For a line load  $q(x)$ , the full flexural response  $w(x)$  is given by the summation of these solutions. For a given surface load, the wavelength and amplitude of the bending vary with the plate's elastic thickness ( $T_e$ ). This methodology is described in detail in [18].

Though the elastic formalism presented above explains reasonably well the bending of an oceanic lithosphere entering a subduction zone, its applicability to FTBs developing adjacent to orogenic domains is debatable. Indeed, in these domains where warmer geotherms are expected, the isostatic

response to loading is—at least in part—accommodated by viscous mass redistributions inside and/or below the plate (e.g., [19, 20]). Isostatic glacial rebound demonstrates the importance of viscous flow in the sublithospheric mantle. The rate of isostatic postglacial uplift, from a few  $\text{mm yr}^{-1}$  to a few  $\text{cm yr}^{-1}$  [21–23], is comparable to tectonic loading rates. To properly capture the magnitude and wavelength of isostatic subsidence, numerical models of FTBs must include the entire lithosphere as well as a layer of asthenosphere of significant thickness (i.e., a total depth of 200–250 km). Typically, the isostatic boundary condition attached to the base of the computational grid allows the asthenosphere to flow in-and-out to maintain the pressure at the base of the model constant. However, to properly capture in sufficient details the structural architecture of FTBs, and resolve vertical motion of few 100s of meter, our numerical experiments require a computational grid of spatial resolution  $< 100$  m. The combination of these two requirements (model 200–250 km deep and grid resolution  $< 100$  m) is out of reach of most advanced numerical codes. Therefore, in our numerical experiments of FTBs, we implement a boundary condition directly underneath the FTB that mimic Airy-like isostasy. For this, we use a high-viscosity virtual layer at the base of the model and a boundary condition at the base of the computational grid allowing that layer to move down and out of the computational domain to maintain the basal pressure constant. The subsidence of the virtual viscous layer captures the integrated viscous flow anywhere in the lithosphere and the subjacent asthenosphere that accommodates isostasy (Figure 1). As the magnitude of the subsidence and its wavelength is a function of the density of the virtual high-viscosity layer, we can explore a range of an Airy-like isostasy by simply varying the density of the high-viscosity layer.

In what follows, we explore how the interaction between horizontal mass transfer, related to tectonic processes, and vertical mass transfer, related to either elastic flexure or viscous flow, impacts the overall architecture of FTBs. We present a series of numerical experiments where the progressive stacking of thrust sheets occurs under contrasting isostatic mechanisms. To simulate isostasy, we use two distinct basal boundary conditions to mimic the elastic bending of the lithosphere or its subsidence in response to the ductile flow. Our experiments illustrate how different modes of isostasy influence the architecture of FTBs.

## 2. Experiment Setup and Numerical Approximations

Our numerical experiments solve the conservation of energy, mass, and momentum equations on a cartesian grid, using *Underworld*, a coupled thermomechanical code [24–26]. The governing equations and numerical method are described in detail in [24]. In our experiments, the numerical domain is 64 km long and 16 km deep, with a grid resolution of 80 m. Model materials are elastic-viscoplastic, and we disregard the role of temperature and strain rate on the viscosity as FTBs form under moderate temperatures. In the formulation of plastic rheology, cohesion and coefficient of friction evolve

TABLE 1: Rheological parameters for numerical experiments. \*Density of the basal layer is 10,000, 4,000, and 3,200 kg m<sup>3</sup> for experiments DF1, DF2, and DF3, respectively.

Material	Density (kg m <sup>-3</sup> )	$\epsilon$ 1	$\epsilon$ 2	Shear modulus (Pa)	Viscosity (Pa s)	Cohesion (MPa)	Cohesion after weakening (MPa)	Friction coefficient	Friction coefficient after weakening
Sticky air	1	N.A.	N.A.	N.A.	$5 \times 10^{18}$	N.A.	N.A.	N.A.	N.A.
Noncohesive sediment	2000	0	0.25	NA	$1 \times 10^{20}$	0	0	0.1	0.01
Sediment A	2600	0	0.25	$2 \times 10^9$	$1 \times 10^{22}$	5	0.5	0.1	0.01
Sediment B	2300	0	0.25	$2 \times 10^9$	$5 \times 10^{20}$	5	0.5	0.1	0.01
Basement	2720	0.1	0.25	$2 \times 10^9$	$1 \times 10^{23}$	40	4	0.6	0.06
Basal layer	*	N.A.	N.A.	N.A.	$1 \times 10^{23}$	N.A.	N.A.	N.A.	N.A.

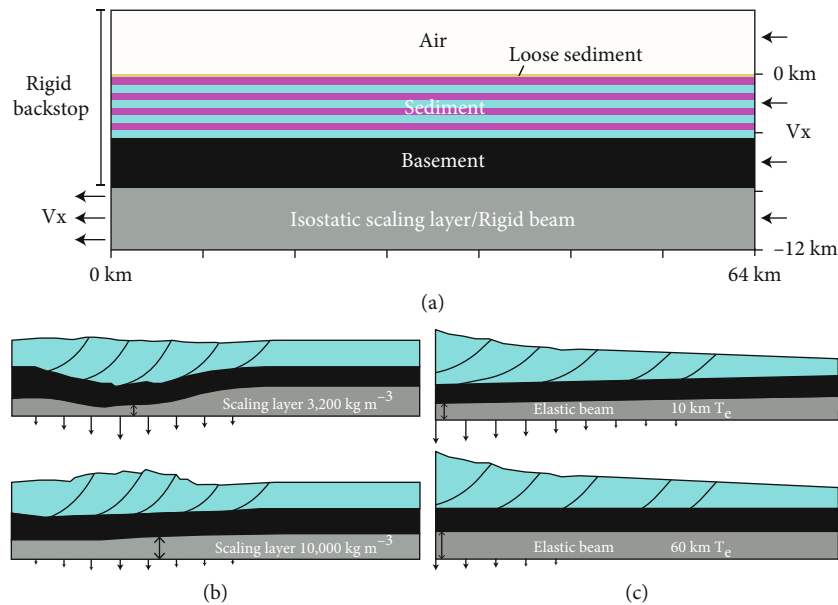


FIGURE 2: (a) Setup and boundary conditions for our numerical models. The basal isostasy boundary condition simulates either (b) Airy-like isostasy mechanism, in which subsidence scales with the density of the basal scaling layer, or (c) elastic flexure, in which subsidence scales with the elastic thickness.

to account for strain-weakening. Material properties are listed in Table 1. Our rheological parameters deliver experimental outcomes reasonably similar to natural examples and consistent with other studies [8, 27–29].

From top to bottom, the model consists of “sticky air” [30], 200 m of “loose sediment” (cohesion of 0 Pa), 4 km of sedimentary rock made up of eight layers of equal thickness but contrasting competence, a 3 km thick basement, and an underlying 4 km thick basal layer (Figure 2). At the top of the model, we impose a free slip condition. Material enters from the right wall at a rate of 1 cm yr<sup>-1</sup> with no slip in the vertical direction. On the left wall, material below the basement is evacuated horizontally at a rate of 1 cm yr<sup>-1</sup>. Above the basement, the left wall acts as a rigid backstop. We apply our isostasy boundary conditions (flexural or ductile flow) to the base of the model.

We run two suites of models using either flexural isostasy or ductile flow isostasy. In alignment with previous studies (e.g., [6, 16, 17]), we simulate isostatic flexure with an elastic beam formulation at the base of the model

(Figure 2(b)). We use GFlex, a widely used flexural response model [18], to calculate the amount of flexure at each model timestep and use that to displace the model vertically. In line with other studies, Young’s modulus ( $7 \times 10^{10}$  Pa) and Poisson’s ratio (0.25) are held constant, and we run experiments with varying  $T_e$ .

For models where isostasy is accommodated by viscous flow, we use an Airy-like boundary condition at the base of the model. This condition maintains constant basal pressure by kinematically evacuating material from the isostatic scaling layer and through the base of the computational grid, allowing the model to subside in response to surface loading. The magnitude and wavelength of the subsidence are controlled by the density of the basal layer. The higher the density is, the smaller the ductile outward flow needed to maintain the basal pressure, and therefore, the lesser the subsidence and the longer its wavelength (Figure 2(c)). A limitation of this approach is that there is no isostatic compensation postthickening. Erosional processes are accounted for via slope instabilities and a hillslope diffusive law, with a

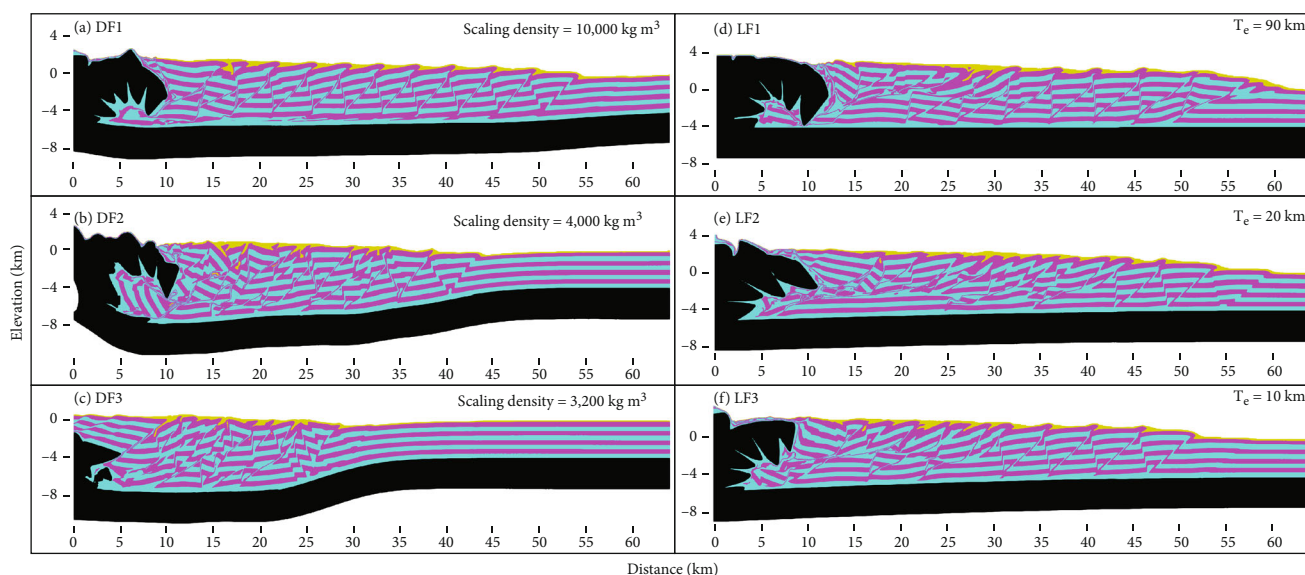


FIGURE 3: Model compositions after 2.1 million years (m.y.) of shortening at  $1 \text{ cm yr}^{-1}$ . DF1-DF3 use the Airy-like ductile flow isostasy condition, and LF1-LF3 use the lithospheric flexure boundary condition.

diffusion coefficient of  $1 \text{ m}^2 \text{ yr}^{-1}$ . We present six key models from two series of numerical experiments (see complete set in the supplementary section). Models LF1-LF3 use the elastic flexure isostasy condition, and DF1-DF3 use the Airy-like ductile flow condition. Experiments DF1 and DF3 deliver smaller/higher subsidence over longer/shorter wavelength, respectively. Experiments LF1 and LF3 have smaller  $T_e$  and larger  $T_e$  and therefore a larger and smaller flexural response, respectively. Experiments DF2 and LF2 are intermediate scenarios. Experiments are compared after reaching 21 km of shortening (approx. 33% shortening). Experiments are evaluated in terms of their topography, internal structure, faults development, stress, and strain rate.

### 3. Results

#### 3.1. Ductile Flow Airy-Like Isostasy Models

**3.1.1. Model DF1—Smaller Subsidence and Longer Wavelength.** This numerical experiment (Figure 3(a)) approximates the situation of a stronger, more viscous lithosphere. Applying a scaling density of  $10,000 \text{ kg m}^{-3}$  to the basal layer delivers a smaller isostatic subsidence and an enhanced subsidence wavelength. In this experiment, the FTB forms above a basement, which remains subhorizontal. Faults form in sequence from the hinterland (to the left) to foreland (to the right). Individual faults are short-lived and accommodate little shortening before becoming inactive (Figures 4(a) and 5(a)). The basement is minimally deformed and is detached from the overlying sedimentary sequence, which accommodates most of the shortening. The stacking sediments into an FTB generate approximately 2 km of topography, which tapers down towards the leading fault. Towards the hinterland, the fold belt develops a gravitationally unstable high topography, which results in gravity-driven faulting and reactivation of older faults.

#### 3.1.2. Model DF3—Larger Subsidence and Shorter Wavelength.

This experiment (Figure 3(c)) approximates the situation of a weaker, less viscous lithosphere. A scaling density of  $3200 \text{ kg m}^{-3}$  to the basal layer enables a larger subsidence over a shorter wavelength. The outcome is an FTB which is narrower compared to experiment DF1, as deformation is localized to a narrower region of intense shortening and deformation. While the sedimentary stack is thickened by about 2 km, its topography is no more than a few hundred meters due to the strong subsidence of the basement. A set of near vertical faults accommodate the differential vertical motions associated with isostatic adjustment. These steeply dipping faults interfere with the set of structures that accommodate horizontal shortening. In addition, the sequence of thrusts that develop in the cover sequence consists of back thrusts and out-of-order thrusts, which complicates the FTB's architecture (Figures 4(c) and 5(c)). This contrasts with the simpler in-sequence thrusting documented in experiment DF1 and suggests that Airy-like ductile isostasy may have a distinct structural signature.

**3.1.3. Model DF2—Intermediate Model.** In this experiment, the scaling density is  $4000 \text{ kg m}^{-3}$  (Figure 3(b)). The magnitude and the wavelength of the subsidence fall in between the two previously discussed end-member experiments. Experiment DF2 produces up to 500 m in topography and a relatively narrow FTB, compared to experiment DF1 but wider compared to experiment DF3. The basement subsides as thrust sheets stack. Gravitational instabilities and gravity-related faulting add to the structural complexity. Subsidence is maximized underneath the load created by the overturned basement nappes.

#### 3.2. Flexural Isostasy Models

**3.2.1. Model LF1—High Lithospheric Elastic Thickness.** Model LF1 (Figure 3(d)) has a  $T_e$  of 90 km (quarter-wavelength of



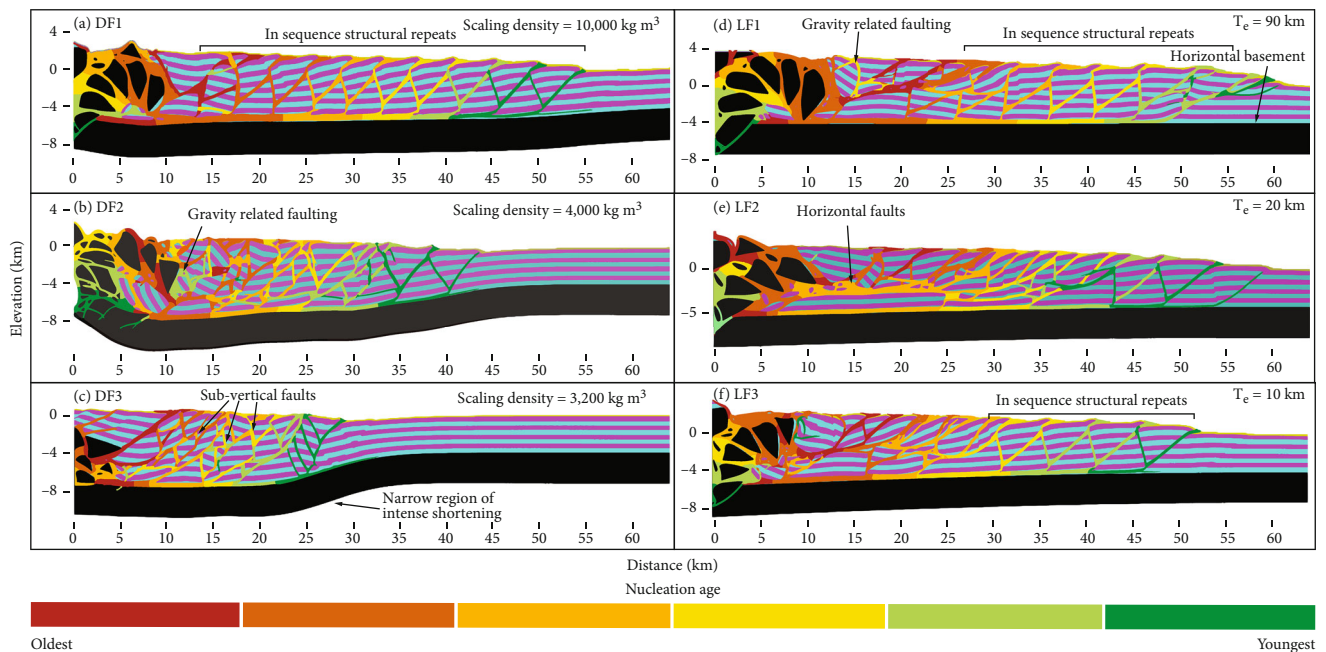


FIGURE 4: Model results with faults colored by nucleation age.

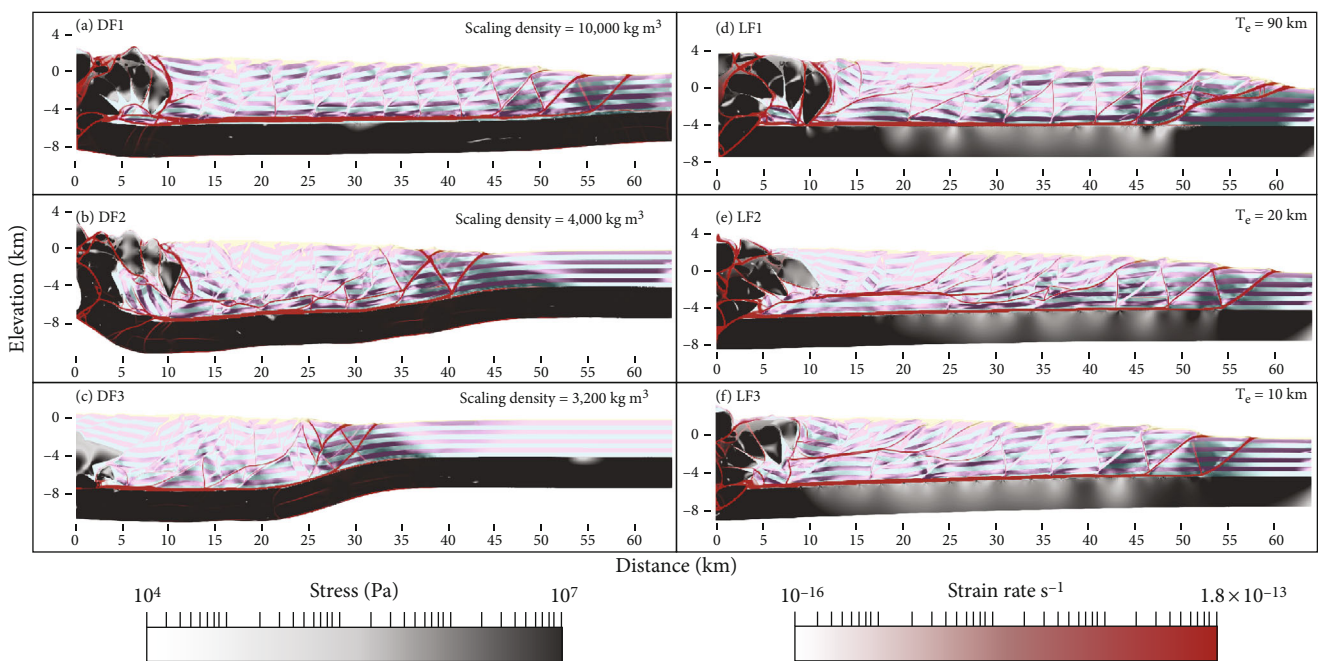


FIGURE 5: Model results highlighting deviatoric stress in grey shading and strain rate in red.

242 km). This model represents the end-member scenario where the tectonic loading exceeds the vertical accommodation space created by flexure. The thrust system generally forms in sequence. Due to the high elastic thickness, the basement retains its initial horizontal profile. This experiment produces approximately 3.5 km of topography, with minimal basement flexure. The high topography towards the backstop produces a gravitational instability and collapse, which contributes to the structural complexity of this model towards the hinterland.

**3.2.2. Model LF3—Small Lithospheric Elastic Thickness.** Model LF3 (Figure 3(f)) has a  $T_e$  of 10 km (quarter-wave-length of 47 km). Here, the small elastic thickness of the lithosphere allows the basement to easily flex as the FTB load is emplaced. Faults form in sequence from hinterland to foreland with relatively little complexity. This model generates approximately 2 km of topography and undergoes a maximum subsidence of approximately 1.3 km near the left wall. The low topography of the model inhibits the

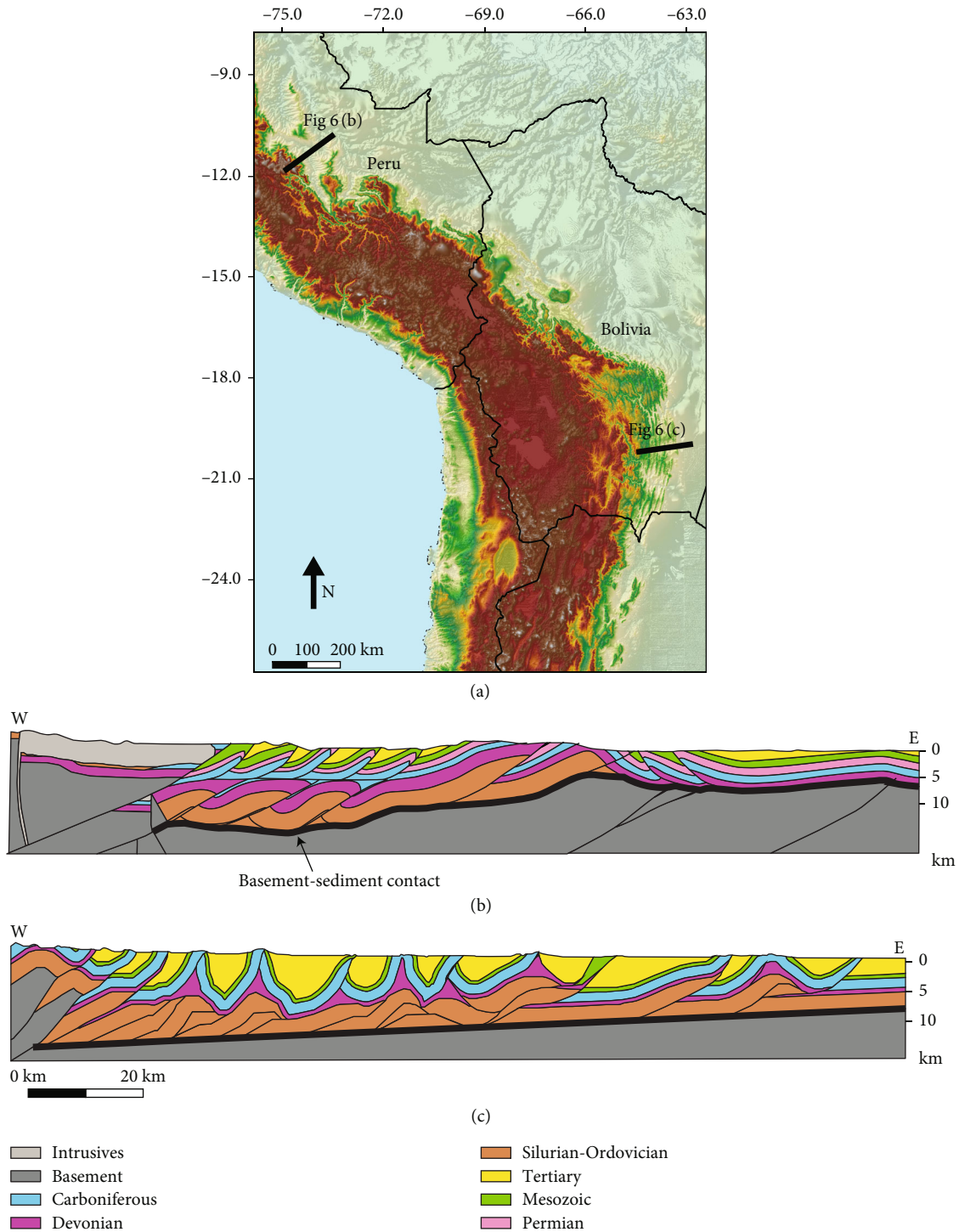


FIGURE 6: (a) Digital elevation map (GTOPO30) of the South American Andes showing locations for section lines in (b) and (c). (b) Cross-section across the Peruvian Subandean zone, modified from Pfiffner and Gonzalez [41]. (c) Cross-section across the Bolivian Subandean zone, modified from Rocha and Cristallini [44]. These cross-sections document the contrasting geometry of the basement-sediment contact.

formation of gravitational instabilities to the extent seen in model LF1.

**3.2.3. Model LF2—Intermediate Lithospheric Elastic Thickness.** This experiment (Figure 3(e)) represents an intermediate scenario between the two previous endmembers. LF2 has a  $T_e$  of 20 km (quarter-wavelength of 78 km), allowing the

model to flex as a response to the FTB load, resulting in approximately 2.4 km of topography. The deformation style of this experiment becomes simpler later in its evolution and towards the foreland and consists of structural repeats. Large horizontal faults cut across many preexisting faults. Toward the model's foreland, younger faults detach along these decollement zones (Figures 4(e) and 5(e)).

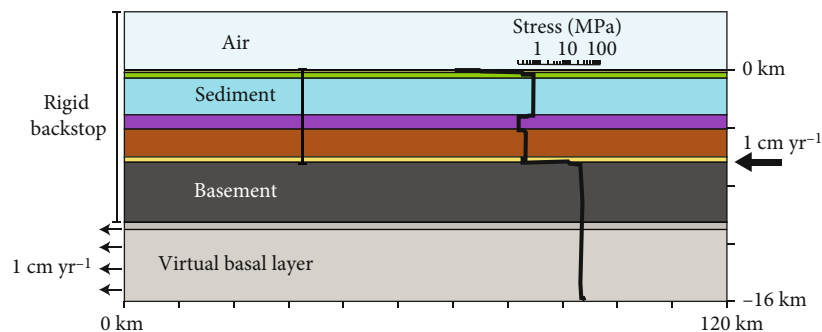


FIGURE 7: Model setup and boundary conditions for models A and B used in the case study of the Subandean zone.

TABLE 2: Rheological parameters for Subandean experiments. \*Density of the basal layer is 3,900 and 10,000 kg m<sup>3</sup> for models A and B, respectively.

Material	Density (kg m <sup>-3</sup> )	$\epsilon$ 1	$\epsilon$ 2	Shear modulus (Pa)	Viscosity (Pa s)	Cohesion (MPa)	Cohesion after weakening (MPa)	Friction coefficient	Friction coefficient after weakening
Sticky air	1	N.A.	N.A.	N.A.	$1 \times 10^{18}$	N.A.	N.A.	N.A.	N.A.
Noncohesive sediment	2000	0	0.25	NA	$1 \times 10^{19}$	0	0	0.01	0.001
Sandstone 1	2600	0	0.25	$2 \times 10^9$	$1 \times 10^{21}$	5	0.1	0.01	0.01
Sandstone 2	2600	0	0.25	$2 \times 10^9$	$1 \times 10^{21}$	5	0.1	0.01	0.01
Shale	2200	0	0.25	$2 \times 10^9$	$5 \times 10^{19}$	5	0.5	0.1	0.01
Sandy shale	2600	0	0.25	$2 \times 10^9$	$1 \times 10^{21}$	1	0.1	0.05	0.005
Basal detachment	2600	0	0.25	N.A.	$5 \times 10^{19}$	5	0.5	0.1	0.01
Basement	2720	0.1	0.25	N.A.	$1 \times 10^{23}$	40	4	0.6	0.06
Basal layer	*	N.A.	N.A.	N.A.	$1 \times 10^{23}$	N.A.	N.A.	N.A.	N.A.

**3.3. Discussion.** In the ductile flow, Airy-like, and suite of models, while all experiments develop an in-sequence thrust system verging towards the foreland, the isostatic adjustment tends to impede the outward propagation of FTBs. High strain rate regions, documenting the active deformation front, are further towards the foreland as the isostatic rate decreases (Figures 5(a)–5(c)). Consequently, when FTBs are associated to a strong subsidence driven by localized ductile flow isostasy, FTBs tend to be narrower, less elevated, and thicker. A stronger subsidence also gave rise to more complex FTB architecture as thrust faults are active longer, accommodating more shortening over a smaller region, and do not conform to a simple in-sequence kinematic (Figure 4). In these fold belts, a set of vertical faults accommodates isostatic subsidence.

Conversely, in the flexural isostasy suite of models, we found that an increase in flexural subsidence does not correspond to an increase in structural complexity. However, similarly to the Airy-isostasy models, when high topographies develop (for high  $T_e$ ), gravitational instability and collapse near the hinterland of the models contribute to a higher structural complexity. A key difference between the two modes of isostasy is the relatively planar basement profile that results from the flexural isostasy condition, compared to the Airy-isostasy. This simpler basement profile

likely encourages the propagation of bedding-parallel faults (i.e., décollement) that are absent in the Airy-like suite of models with a high isostatic rate. This suggests that décollement may be signature of FTBs that form under high  $T_e$  or low isostatic subsidence rate conditions, whereas vertical faulting may be signature of a relatively high isostatic rate due to a more ductile basement.

**4. Application to the Subandean Zone Fold and Thrust Belts**

While 2-D numerical experiments cannot capture the diversity and range of complexity that exists in nature, insights from our numerical experiments can nevertheless tentatively be applied to natural examples. Here, we compare our results with the Subandean FTB (Figure 6). Along the South American Cordillera, the Neogene Subandean zone is the transitional region between the Cordillera’s elevated hinterland and the undeformed platform of the South American continent. Along the Subandean zone, the  $T_e$  varies from a maximum of ~90 km in the bend region of the Andes within Bolivia (latitude of 20°S), to a minimum of ~10 km away from the bend region towards Peru to the north and Argentina to the south (approx. latitudes 13°S and 25°S, respectively) [31, 32]. This change in  $T_e$  correlates with strong

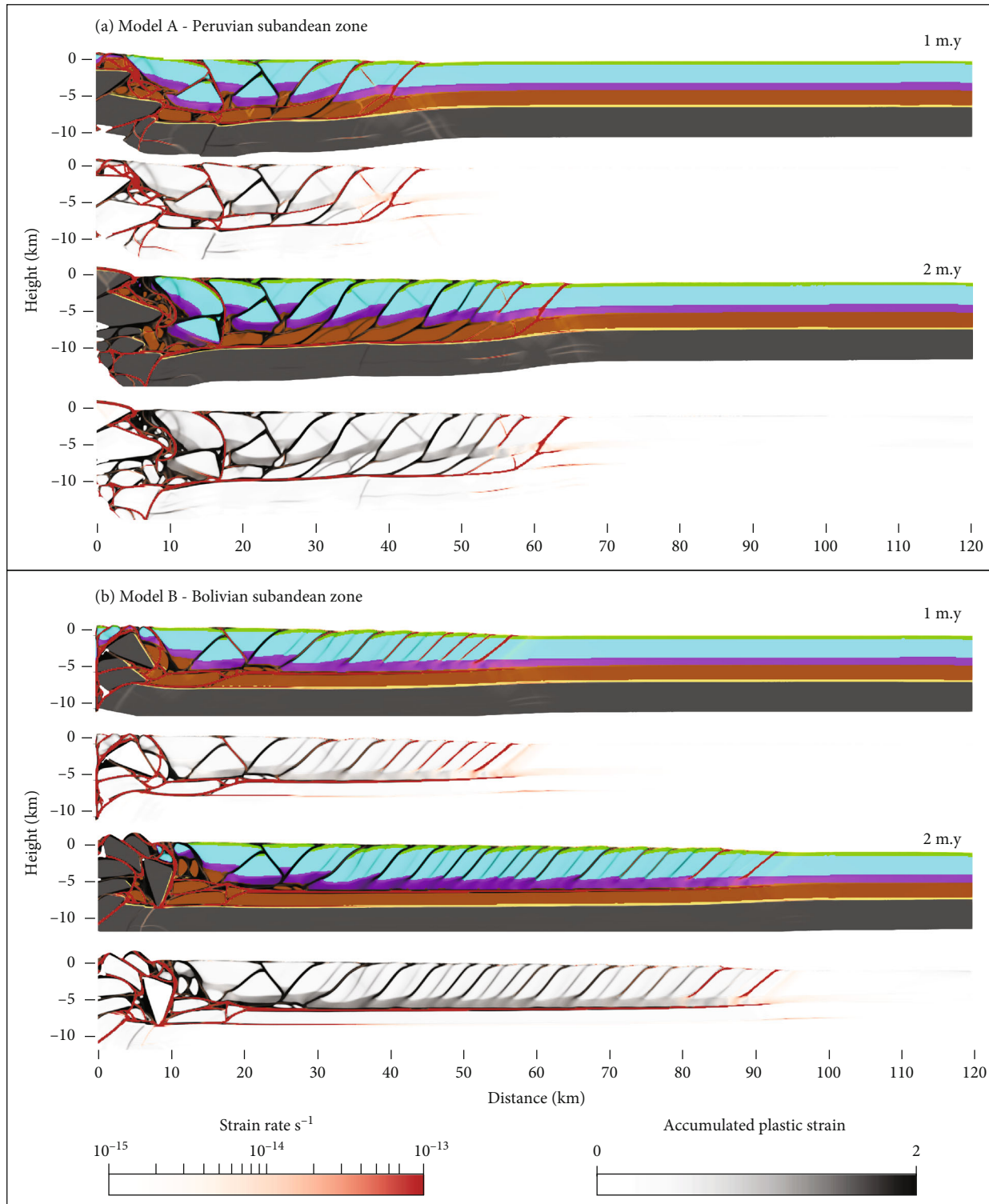


FIGURE 8: Model results after 1 m.y. and 2 m.y. of shortening. The accumulated plastic strain (in black) highlights inactive faults, and areas of high strain rate represent active faults. (a) Model A has a high isostatic subsidence rate, approximating the Peruvian Subandean zone. (b) Model B has a low isostatic subsidence rate approximating the Bolivian Subandean zone.

variations in surface heat flow [32]. Hence, this region is ideal to assess how the strength of a plate impacts the development of FTBs, via the modulation of isostasy. In a pioneer study, [31] noted that in parts of the Andes where a high  $T_e$

minimizes isostatic flexure, fold belts are wider and structurally simpler compared to regions where  $T_e$  is lesser. More recently, [32] reemphasize this point, finding a strong correlation between structural style and  $T_e$ . Additionally, ductile



flow of the lower crust [33] and mantle [34] influence how shortening is accommodated across the Andes. Ouimet and Cook [35] have suggested that there is redistribution of material in the lower crust through ductile flow, related to crustal thickening and surface uplift. Postseismic uplift reveals mantle and lower crust viscosities as low as  $10^{18}$  Pa s in parts of the Andes [36, 37].

The Peruvian Subandean zone overlies a relatively weak lithosphere with a  $T_e$  of 10 to 20 km [38, 39]. Moreover, parts of the Peruvian Andes are in isostatic equilibrium at the Moho [40]. The weak lithosphere paired with a slow convergence rate makes this area an ideal case study for the scenario in which isostatic subsidence keeps up with the tectonic loading. This region has accommodated up to 40 km of shortening and is characterized by thin-skinned imbricate thrusting [41], disharmonic folding, back thrusts, and triangle zones [42]. In this region, the basement has recorded a strong subsidence localized where the imbricate stack of thrust sheets is at its thickest (Figure 6(b)). Our numerical experiment DF3 suggests that this strong localized subsidence could be accommodated by ductile flow in the basement, rather than elastic flexure. The geometry of the basement-FTB contact contrasts with that observed further south in the Bolivian Subandean zone.

In the Bolivian Subandean zone (Figure 6(c)),  $T_e$  increases between 40 and 90 km [32], in a region that was shortened by approximately 40% over the last 12 m.y. [43]. The FTB architecture consists of lateral structural repetition of decreasing age in the direction of propagation [43]. Locally, structural complexities derive from the activation of multiple decollement levels [44]. Unlike the Peruvian Subandean zone, the cover is entirely detached from the basement, the surface of which is planar and gently tilted towards the hinterland. The Bolivian Subandean zone is approximately 30% wider than the Peruvian Subandean zone. These attributes are consistent with numerical experiment DF1 and LF1, which suggests that, in the Bolivian Subandean zone, ductile flow in the basement may not be important.

To test this idea, we designed two numerical models (models A and B) that approximate the thickness and stratigraphy of the Subandean zone. Both models use the Airy-style isostasy condition to test the role of ductile flow in the structuration of the Subandean zone. In model A, we maximize ductile flow and isostatic subsidence to reflect the Peruvian Subandean zone, and in model B, we minimize ductile flow and subsidence to reflect the Bolivian Subandean zone. The material and rheological setups between models A and B were held constant to isolate the effect of ductile flow on FTB evolution. The material setup and boundary condition of these models are summarized in Figure 7 and Table 2.

Model A (Figure 8(a)), in which isostasy subsidence keeps up with the tectonic loading, shares key features with its Peruvian analogue. In particular, the basement records a strong subsidence underneath a relatively narrower FTB. Shortening in the FTB is accommodated by imbricated thrust, steepening faults, pop-up and pop-down structures, and back thrust. In comparison, model B (Figure 8(b)),

which reflects a less ductile Bolivian zone, displays gently sloping top basement profile, over which a wider, structurally simpler FTB evolves through the progressive lateral propagation of structural repetition towards the foreland.

Our models do not attempt to capture the details of the structural architecture of the FTBs in the Bolivian and Peruvian Subandean zones. However, the geometry of the basement-basin interfaces is reproduced to the first order and agrees with the proposition that strong subsidence underneath an FTB can be explained by ductile flow in the basement.

## 5. Conclusions

Our numerical experiments confirm that the structural architecture of FTBs is sensitive to the interplay between the vertical motions induced by isostasy and the horizontal motions due to tectonics. They also show that the mode of isostasy is a critical to the development of FTB. Our experiments show that when isostasy is accommodated by viscous flow, subsidence beneath the surface load is localized, impeding the outward propagation of the FTB and limiting topography. This leads to narrower and structurally more complex FTBs, in which steeply dipping faults accommodate a stronger subsidence. When viscous flow is subdued and subsidence is less important, FTBs propagate farther outwards via the lateral repetition of simpler structures. Importantly, the smaller isostatic subsidence leads to higher topography. We conclude that in FTBs associated to orogenic systems, viscous flow plays an important role in their development. For more rigid lithospheres, where isostasy is better described by lithospheric flexure, we found that a change in  $T_e$  and therefore a change in flexure play a lesser role in the structural style of FTBs. Nevertheless, larger  $T_e$  delivers FTB with higher topography, with increased erosion and sediment flux, into adjacent basins.

## Data Availability

Data supporting the results can be found in the manuscript text, figures, and discussed references. The underlying open-source framework Underworld used to run our models can be found here doi:10.5281/zenodo.1436039. Input scripts are available at doi:10.5281/zenodo.6629741.

## Disclosure

An earlier iteration of this manuscript was presented at a conference here doi:10.5194/egusphere-egu21-13767.

## Conflicts of Interest

The authors declare that there is no conflict of interest regarding the publication of this paper.

## Acknowledgments

This research was supported by the National Computational Infrastructure (NCI), through the National Computational Merit Allocation Scheme, the Pawsey Supercomputing

Centre with funding from the Australian Government and the Government of Western Australia, and Australian Research Council grants ARC-IH130200012 and ARC-LP190100146. We thank J. Giordani and Dr. R. Beucher for their expert support with Underworld and two anonymous reviewers for contributing to greatly improve the manuscript.

## References

- [1] E. J. Teresa, "Thrust loads and foreland basin evolution, cretaceous, Western United States," *American Association of Petroleum Geologists Bulletin*, vol. 65, 1981.
- [2] G. D. Karner and A. B. Watts, "Gravity anomalies and flexure of the lithosphere at mountain ranges," *Journal of Geophysical Research - Solid Earth*, vol. 88, no. B12, pp. 10449–10477, 1983.
- [3] J. Toth, N. J. Kusznir, and S. S. Flint, "A flexural isostatic model of lithosphere shortening and foreland basin formation: application to the Eastern Cordillera and Subandean belt of NW Argentina," *Tectonics*, vol. 15, no. 1, pp. 213–223, 1996.
- [4] S. Hoth, A. Hoffmann-Rothe, and N. Kukowski, "Frontal accretion: an internal clock for bivergent wedge deformation and surface uplift," *Journal of Geophysical Research*, vol. 112, no. B6, 2007.
- [5] J. Malavieille and E. Konstantinovskaya, "Impact of surface processes on the growth of orogenic wedges: insights from analog models and case studies," *Geotectonics*, vol. 44, no. 6, pp. 541–558, 2010.
- [6] C. Fillon, R. S. Huismans, and P. P. van der Beek, "Syntectonic sedimentation effects on the growth of fold-and-thrust belts," *Geology*, vol. 41, no. 1, pp. 83–86, 2013.
- [7] E. Saura, D. Garcia-Castellanos, E. Casciello, V. Parravano, A. Urruela, and J. Vergés, "Modeling the flexural evolution of the Amiran and Mesopotamian foreland basins of NW Zagros (Iran-Iraq)," *Tectonics*, vol. 34, no. 3, pp. 377–395, 2015.
- [8] J. B. Ruh and J. Vergés, "Effects of reactivated extensional basement faults on structural evolution of fold-and-thrust belts: insights from numerical modelling applied to the Kopet Dag Mountains," *Tectonophysics*, vol. 746, pp. 493–511, 2018.
- [9] A. J. Cawood and C. E. Bond, "3D mechanical stratigraphy of a deformed multi-layer: linking sedimentary architecture and strain partitioning," *Journal of Structural Geology*, vol. 106, pp. 54–69, 2018.
- [10] T. L. Pavlis, M. W. Hamburger, and G. L. Pavlis, "Erosional processes as a control on the structural evolution of an actively deforming fold and thrust belt: an example from the Pamir-Tien Shan region, Central Asia," *Tectonics*, vol. 16, no. 5, pp. 810–822, 1997.
- [11] O. Pla, E. Roca, H. Xie et al., "Influence of syntectonic sedimentation and décollement rheology on the geometry and evolution of orogenic wedges: analog modeling of the Kuqa fold- and-thrust belt (NW China)," *Tectonics*, vol. 38, no. 8, pp. 2727–2755, 2019.
- [12] R. W. H. Butler, "Syn-kinematic strata influence the structural evolution of emergent fold-thrust belts," *Geological Society - Special Publications*, vol. 490, no. 1, pp. 57–78, 2020.
- [13] F. A. Dahlen, J. Suppe, and D. Davis, "Mechanics of fold-and-thrust belts and accretionary wedges: cohesive coulomb theory," *Journal of Geophysical Research*, vol. 89, no. B12, pp. 10087–10101, 1984.
- [14] F. Storti and K. McClay, "Influence of syntectonic sedimentation on thrust wedges in analogue models," *Geology*, vol. 23, no. 11, pp. 999–1002, 1995.
- [15] G. S. Stockmal, C. Beaumont, M. Nguyen, and B. Lee, "Mechanics of thin-skinned fold-and-thrust belts: insights from numerical models," in *Special Paper 433: Whence the Mountains? Inquiries into the Evolution of Orogenic Systems: A Volume in Honor of Raymond A. Price*, pp. 63–98, GSA Special Papers, 2007.
- [16] S. Gradmann, C. Beaumont, and M. Albrecht, "Factors controlling the evolution of the Perdido Fold Belt, northwestern Gulf of Mexico, determined from numerical models," *Tectonics*, vol. 28, no. 2, 2009.
- [17] G. D. H. Simpson, "Influence of the mechanical behaviour of brittle-ductile fold-thrust belts on the development of foreland basins," *Basin Research*, vol. 22, no. 2, pp. 139–156, 2010.
- [18] A. D. Wickert, "Open-source modular solutions for flexural isostasy: gFlex v1.0," *Geoscientific Model Development*, vol. 9, no. 3, pp. 997–1017, 2016.
- [19] S. M. Nakiboglu and K. Lambeck, "A study of the Earth's response to surface loading with application to Lake Bonneville," *Geophysical Journal of the Royal Astronomical Society*, vol. 70, no. 3, pp. 577–620, 1982.
- [20] M. H. P. Bott, "Modeling local crustal isostasy caused by ductile flow in the lower crust," *Journal of Geophysical Research - Solid Earth*, vol. 104, no. B9, pp. 20349–20359, 1999.
- [21] W. R. Peltier, D. F. Argus, and R. Drummond, "Space geodesy constrains ICE age terminal deglaciation: the global ICE-6G\_C (VM5a) model," *Journal of Geophysical Research - Solid Earth*, vol. 120, no. 1, pp. 450–487, 2015.
- [22] J. Mey, D. Scherler, A. D. Wickert et al., "Glacial isostatic uplift of the European Alps," *Nature Communications*, vol. 7, no. 1, pp. 1–10, 2016.
- [23] V. R. Barletta, M. Bevis, B. E. Smith et al., "Observed rapid bedrock uplift in amundsen sea embayment promotes ice-sheet stability," *Science*, vol. 360, no. 6395, pp. 1335–1339, 2018.
- [24] L. Moresi, F. Dufour, and H.-B. Mühlhaus, "A Lagrangian integration point finite element method for large deformation modeling of viscoelastic geomaterials," *Journal of Computational Physics*, vol. 184, no. 2, pp. 476–497, 2003.
- [25] L. Moresi, S. Quenette, V. Lemiale, C. Mériaux, B. Appelbe, and H. B. Mühlhaus, "Computational approaches to studying non-linear dynamics of the crust and mantle," *Physics of the Earth and Planetary Interiors*, vol. 163, no. 1–4, pp. 69–82, 2007.
- [26] R. Beucher, L. Moresi, J. Giordani et al., "UWGeodynamics: a teaching and research tool for numerical geodynamic modelling," *Journal of Open Source Software*, vol. 4, no. 36, p. 1136, 2019.
- [27] M. Bonini, F. Sani, and B. Antonielli, "Basin inversion and contractional reactivation of inherited normal faults: a review based on previous and new experimental models," *Tectonophysics*, vol. 522–523, pp. 55–88, 2012.
- [28] A. Bauville and S. M. Schmalholz, "Transition from thin- to thick-skinned tectonics and consequences for nappe formation: Numerical simulations and applications to the Helvetic nappe system, Switzerland," *Tectonophysics*, vol. 665, pp. 101–117, 2015.
- [29] P. Granado and J. B. Ruh, "Numerical modelling of inversion tectonics in fold-and-thrust belts," *Tectonophysics*, vol. 763, pp. 14–29, 2019.

- [30] F. Crameri, H. Schmeling, G. J. Golabek et al., "A comparison of numerical surface topography calculations in geodynamic modelling: an evaluation of the 'sticky air' method," *Geophysical Journal International*, vol. 189, no. 1, pp. 38–54, 2012.
- [31] A. B. Watts, S. H. Lamb, J. D. Fairhead, and J. F. Dewey, "Lithospheric flexure and bending of the Central Andes," *Earth and Planetary Science Letters*, vol. 134, no. 1-2, pp. 9–21, 1995.
- [32] H. P. A. García, G. M. Gianni, M. N. Lupari et al., "Effective elastic thickness in the Central Andes. Correlation to orogenic deformation styles and lower crust high-gravity anomaly," *Journal of South American Earth Sciences*, vol. 87, pp. 232–246, 2018.
- [33] S. L. Beck and G. Zandt, "The nature of orogenic crust in the Central Andes," *Earth*, vol. 107, no. B10, pp. ESE 7-1–ESE 7-16, 2002.
- [34] F. Shi, S. Li, and M. Moreno, "Megathrust locking and viscous mantle flow induce continental shortening in Central Andes," *Pure and Applied Geophysics*, vol. 177, no. 6, pp. 2841–2852, 2020.
- [35] W. B. Ouimet and K. L. Cook, "Building the central Andes through axial lower crustal flow," *Tectonics*, vol. 29, no. 3, article TC3010, 2010.
- [36] G. Luo and M. Liu, "How does trench coupling lead to mountain building in the Subandes? A viscoelastoplastic finite element model," *Journal of Geophysical Research*, vol. 114, no. B3, article B03409, 2009.
- [37] S. Li, M. Moreno, J. Bedford et al., "Postseismic uplift of the Andes following the 2010 Maule earthquake: implications for mantle rheology," *Geophysical Research Letters*, vol. 44, 2017.
- [38] A. Tassara, C. Swain, R. Hackney, and J. Kirby, "Elastic thickness structure of South America estimated using wavelets and satellite-derived gravity data," *Earth and Planetary Science Letters*, vol. 253, no. 1-2, pp. 17–36, 2007.
- [39] V. Sacek and N. Ussami, "Reappraisal of the effective elastic thickness for the sub-Andes using 3-D finite element flexural modelling, gravity and geological constraints," *Geophysical Journal International*, vol. 179, no. 2, pp. 778–786, 2009.
- [40] C. Condori, G. S. França, H. J. Tavera, D. F. Albuquerque, B. T. Bishop, and S. L. Beck, "Crustal structure of North Peru from analysis of teleseismic receiver functions," *Journal of South American Earth Sciences*, vol. 76, pp. 11–24, 2017.
- [41] O. A. Pfiffner and L. Gonzalez, "Mesozoic Cenozoic evolution of the western margin of South America: case study of the Peruvian Andes," *Geosciences*, vol. 3, no. 2, pp. 262–310, 2013.
- [42] N. Espurt et al., "Paleozoic structural controls on shortening transfer in the Subandean foreland thrust system, Ene and southern Ucayali basins, Peru," *Tectonics*, vol. 27, pp. 1–21, 2008.
- [43] Á. Sánchez, A. M. Goncalves, K. Asquith, and K. Hill, "Kinematic deformation model of the south-central subandean zone, Bolivia," *Journal of South American Earth Sciences*, vol. 103, article 102768, 2020.
- [44] E. Rocha and E. O. Cristallini, "Controls on structural styles along the deformation front of the Subandean zone of southern Bolivia," *Journal of Structural Geology*, vol. 73, pp. 83–96, 2015.